Plasmon-Driven Photocatalysis Leads to Products Known from E-beam and X-ray-Induced Surface Chemistry

Plasmon-driven photocatalysis leads to products known from e-beam and x-ray-induced surface chemistry

Jacek Szczerbiński, Luzia Gyr, Jérôme Kaeslin and Renato Zenobi*

Department of Chemistry and Applied Biosciences, Laboratory of Organic Chemistry, ETH Zurich, 8093 Zurich, Switzerland, e-mail: zenobi@org.chem.ethz.ch

Abstract

Plasmonic metal nanostructures can concentrate incident optical fields in nanometer-sized volumes, called hot spots. This leads to enhanced optical responses of molecules in such a hot spot, but also to chemical transformations, driven by plasmon-induced hot carriers. Here, we employ tip-enhanced Raman spectroscopy (TERS) to study the mechanism of these reactions *in situ*, at the level of a single hot spot. Direct spectroscopic measurements reveal the energy distribution of hot electrons, as well as the temperature changes due to plasmonic heating. Therefore, charge-driven reactions can be distinguished from thermal reaction pathways. The products of the hot-carrier-driven reactions are strikingly similar to the ones known from x-ray or e-beam-induced surface chemistry, despite the >100-fold energy difference between visible and x-ray photons. Understanding the analogies between those two scenarios implies new strategies for rational design of plasmonic photocatalytic reactions and for the elimination of photoinduced damage in plasmon-enhanced spectroscopy.

Keywords: hot electrons, plasmon-driven photocatalysis, tip-enhanced Raman spectroscopy, photoinduced damage, desorption induced by electronic transitions

TOC Graphic

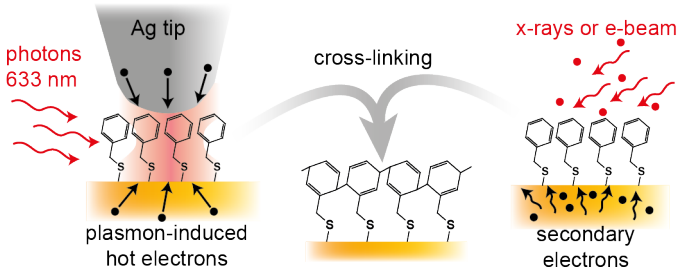

Introduction

Plasmonic nanostructures illuminated with visible light can catalyze chemical reactions of adsorbed molecules. Examples of plasmonically accelerated industrially relevant reactions include water splitting[1,2], CO oxidation[3], ethylene epoxidation[4,5] and decomposition of organic compounds in wastewater[6]. Enhancement of the reaction rate by visible light relies on excitation and decay of localized surface plasmons in nanostructured catalysts[7,8]. Plasmon decay can result in enhanced photoemission, or in formation of electron-hole pairs with energies higher than the regular thermal energy (Fig. 1B)[7,9]. Hot electrons can undergo transitions from the metal nanostructure into unoccupied orbitals of adsorbates, generating reactive anions or radicals[6,8].

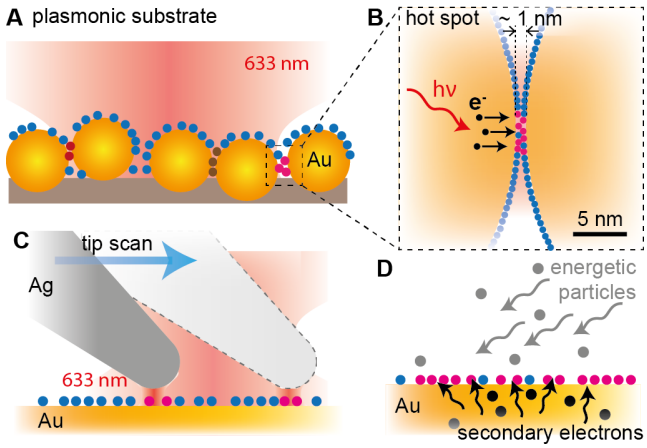

Figure 1. Photochemical reactions in plasmonic hot spots vs. irradiation with energetic particles. (A) Photochemistry on plasmonic substrates occurs in confined volumes with highly enhanced electric fields, called hot spots. The hot spots differ in enhancement and are located randomly on the substrate, at nanometer-sized gaps between nanoparticles. Unreacted molecules are marked in blue, whereas molecules residing in the hot spots are marked with different colors, corresponding to different reaction products. (B) Zoom into a single hot spot. Laser photons couple to the electrons in the metal, forming plasmons. Non-radiative decay of the plasmons results in formation of hot electrons (black dots) that undergo transitions into unoccupied orbitals of adsorbed molecules. (C) In tip-enhanced Raman spectroscopy (TERS), photochemistry can be studied at a single location, *i. e.* the hot spot formed between

a plasmonic tip and a flat substrate. The tip can be scanned over the surface, such that different molecules are probed – yet always with the same hot spot. (D) Irradiation of organic monolayers with energetic particles (x-ray photons, <50 eV electrons) induces similar reactions as plasmon-induced hot electrons. Secondary electrons scattered off the metallic substrate play the same role as hot carriers in plasmonic hot spots. In this scenario the reaction happens uniformly all over the sample surface.

Reactivity of metal nanoparticles lies at the heart of research in heterogeneous catalysis[10]. The relationship between the reaction site's structure and reactivity of the reaction site cannot be teased out from ensemble measurements (Fig. 1A), which average data from many reaction sites[11]. Therefore, electron transfer in noble metal nanocatalysts has been extensively studied at the single-particle or single-aggregate level (Fig. 1B), allowing characterization of the reaction sites with nanoscale spatial resolution. Hot electron transport at single plasmonic hot spots has been investigated for numerous model reactions, using various techniques, including surface plasmon resonance spectroscopy[12,13], single-molecule fluorescence microscopy[14–16], surface-enhanced Raman spectroscopy (SERS)[17,18] and microscopy[19], as well as tip-enhanced Raman spectroscopy (TERS)[20–23].

At the same time, a significant effort has been made to understand the competition between charge-driven reactions and plasmonic heating, which compete in plasmon-driven catalysis. Christopher *et al.*[4] distinguished charge-induced reactions from phonon-driven effects in ethylene epoxidation on Ag nanoparticles by measuring steady-state reaction kinetics in chemical reactors. They confirmed the dominant effect of carrier generation, relying on two observations: the presence of a kinetic isotope effect, and a linear dependence of the reaction yields on irradiance. An in-depth study by Zhang *et al.*[24] employed similar methods to study methanation of CO_2 on Rh/TiO_2 particles. Yet, they found a synergy between plasmon-assisted charge transfer and plasmonic

heating. Remarkably, a similar finding was reported by Yu *et al.*[25], who employed scanning electrochemical microscopy to study the electron transfer between Au nanoparticles and ferricyanide ions in confined sub-micrometer volumes under a sharp ultrananoelectrode. Charge- and phonon-driven processes were also disentangled by Zou *et al.*[14] at the level of a single plasmonic hot spot. They quantified the electron transport kinetics for the two contributions by correlating electron microscopic imaging of single aggregates with superresolution fluorescence imaging of the catalytic product.

Single-molecule SERS and TERS seem to be ideally suited for studying plasmon-induced catalysis at the single particle level[20–23], thanks to a number of advantages: (*i*) these techniques provide highly localized spectroscopic signal originating exclusively from the plasmonically active site[26,27], (*ii*) they are not limited to fluorescent reactants/products, (*iii*) the oxidation state and orientation of the reactant can be identified based on the vibrational spectrum[28–30], (*iv*) the identities of the chemical species forming in the plasmonic hot spot can be traced in real time[17], (*v*) the temperature at the reaction site can be quantified at the level of a single hot spot[31–33]. Surprisingly, SERS/TERS studies of plasmon-driven reactions focus only on a narrow range of prototypical reactants. The vast majority of papers concern *para*-nitrothiophenol – which can be reduced to *para*-aminothiophenol[18,34] and further dimerize to dimercaptoazobenzene[17,35–37]. A number of studies describe plasmon-assisted electron transfer in biphenyl and bipirydine derivatives[38–41]. Singular reports have been published for other reactants, *e. g.* oxidation of phenyl isocyanide[42], photodissociation of dimethyl disulfide[43], demethylation of methylene blue[44], or dehydroxylation of *p*-hydroxythiophenol[45]. Presumably, the scope of reactants used in SERS/TERS studies of photocatalysis is so limited, because many industrially relevant molecules are susceptible to photodamage, resulting in contamination (fouling) of the reaction site and unstable spectroscopic signal.

In this contribution, we employ SERS and TERS to address the following questions:

- How to predict the products of plasmon-driven reactions for an arbitrary reactant?
- How to quantify the contributions of carrier generation and plasmonic heating based on direct spectroscopic measurements?
- What is the nature of photodamage in plasmonic hot spots? Why do some samples degrade easily, while other are very stable?

We study seven model molecules, previously known from surface science experiments, with diverse chemical properties. The TERS tip-sample junction acts as a photocatalytic nanoreactor, allowing us to perform *in situ* spectroscopy at the level of a single hot spot (Fig. 1C). We use the Stokes bands of SER/TER spectra to identify the reaction products, and the anti-Stokes (aS) background to measure the ratio between hot and thermally equilibrated electrons. We demonstrate that hot carriers open a broad scope of thermally inaccessible reaction pathways. The non-thermal nature of the reported reactions is confirmed by spectroscopic monitoring of the temperature in the plasmonic hot spot, and additional temperature-programmed desorption mass spectrometry (TPD-MS) measurements. The non-thermal reaction pathways reported in this paper are similar to the ones known from surface science experiments (Fig. 1D), where organic molecules adsorbed on flat metallic substrates are irradiated with x-rays or low energy electrons (<50 eV). Our results indicate that secondary electrons scattered off the substrate upon irradiation with energetic particles have the same effect as hot electrons in plasmon-induced photocatalysis, and lead to similar products. We postulate that this analogy can be extrapolated to other reactants, *ergo* the pathways, energetics and

products of plasmon-driven reactions can be predicted for any reactant, based on the published studies of electron-beam induced reactions for that reactant.

Modification of thiolate SAMs under the TERS tip

In order to separate plasmon-driven reactions from thermally induced processes, we performed SERS and TERS measurements on self-assembled monolayers (SAMs) of thiolates with different desorption temperatures and electron capture cross-sections. Fig. 2 presents the chemical transformations induced by the TERS tip in SAMs of three thiols: 1-hexadecanethiol (HDT, Fig. 2A), biphenyl-4-thiol (BPT, Fig. 2B) and 1H,1H,2H,2H-perfluorodecane-1-thiol (PFDT, Fig. 2C). Pristine monolayers are presented in the lower part of Fig. 2, whereas tentative structures of the reacted SAMs are shown in the upper part of the figure. These three SAMs behave very differently upon irradiation of the plasmonic tip-sample junction.

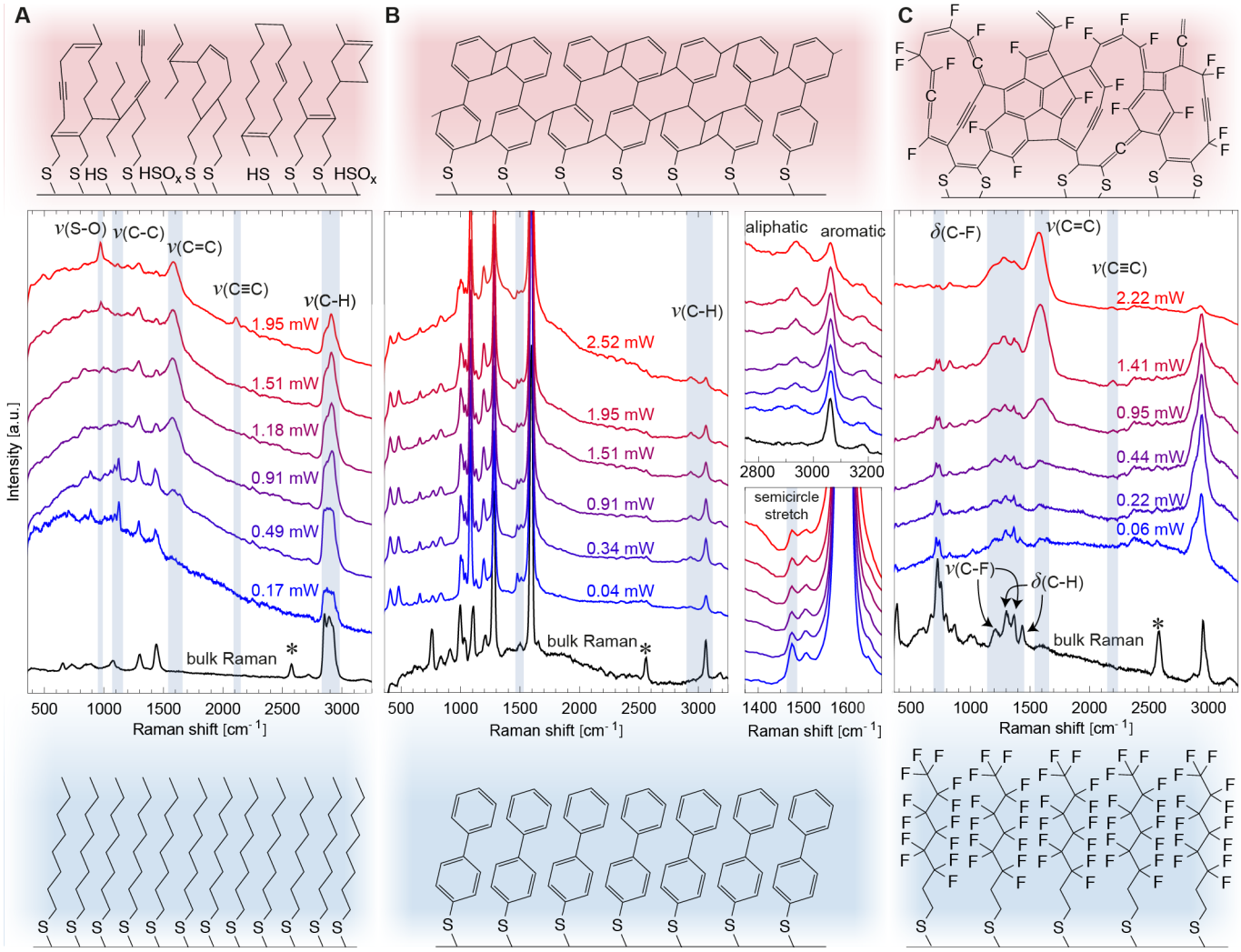

Figure 2. Reactions in organic monolayers triggered by the TERS tip result in similar products as bombarding them with energetic particles. Unreacted SAMs are shown in the lower panels (light blue background), whereas tentative structures of the reacted monolayers are shown in the upper panels (light red background). (A) HDT SAM is subject to dissociation of C-H, C-C and C-S bonds, and to formation of crosslinks within the monolayer. (B) BPT crosslinks with loss of aromaticity, but does not dissociate. (C) PFDT loses fluorine, and soon turns into a disordered mixture of saturated and unsaturated hydrocarbons. For the sake of clarity, the alkyl chains of HDT and PFDT were shortened to eight carbon atoms in the schemes. Details of the TER spectra are discussed in the main text. The ν(S-H) vibration of bulk thiols is marked with an asterisk (∗) and is absent in thiolate SAMs.

The TER spectrum of the HDT SAM acquired at low laser power (0.17 mW, blue line in Fig. 2A) closely resembles the confocal Raman spectrum of HDT (black line), whereas

symptoms of reaction progress arise at higher laser powers. Formation of double bonds in HDT manifests itself by the appearance of the ν(C=C) band at 1580 cm^{-1}. Formation of triple bonds (ν(C≡C) at 2110 cm^{-1}) at the highest laser power is presumably due to further dehydrogenation, similar to a recent TERS study conducted in ultra-high vacuum (UHV)[46]. Formation of crosslinks leads to depletion of the chain vibrations (1060-1140 cm^{-1}). We observe a change of shape of the ν(C-H) band around 2900 cm^{-1}, without appearance of a component above 3000 cm^{-1} (sp^2-hybridized C-H stretches), which indicates that double bonds form crosslinks and are not part of the alkyl chain. At high laser powers, C-S bond scission occurs, followed by oxidation of sulfur left on the surface (sulfate band at 980 cm^{-1}), similar to the effect of SAM removal by ozone[47]. Similar, but more severe, modifications were induced in decanethiol SAMs (Fig. S16).

Formation of crosslinks between phenyl rings of BPT molecules (Fig. 2B) manifests itself in a gradual loss of the semicircle stretch at 1485 cm^{-1} (inset in Fig. 2B), as well as a gradual loss of aromatic C-H vibrations at 3060 cm^{-1}, accompanied by an increase in the aliphatic C-H stretches around 2940 cm^{-1} (inset in Fig. 2B).

TERS experiments performed on PFDT showed symptoms of gradual abstraction of hydrogen and fluorine: appearance of ν(C=C) at 1600 cm^{-1} and ν(C≡C) at 2250 cm^{-1}, loss of δ(C—F) at 740 cm^{-1} and ν(C—F) at 1200 and 1365 cm^{-1}. The SAM turns into an amorphous layer of hydrocarbons, yielding broad carbonaceous bands at 1300 and 1590 cm^{-1}.

The non-thermal nature of the reactions reported above is confirmed by TPD-MS experiments (Fig. S2, S3, S7) performed on SAMs of the same thiolates. Heating the monolayer in the absence of the TERS tip did not induce intermolecular crosslinking, C-S bond scission, loss of fluorine, *etc.*, as shown in the mass spectra of the species desorbed.

The only exception was dehydrogenation of HDT, which was also observed in TPD-MS at temperatures above 450 K (way above the temperature present under the TERS tip, *cf.* Fig. S8). However, this reaction may have occurred in our plasma ionization source, independent of sample desorption (see Fig. S2). Thus, the TPD-MS data proves that the reported reactions in the SAMs are induced by electronic transitions, not by thermal mechanisms.

50 eV electrons vs. visible photons

There is a striking resemblance of the products forming under the TERS tip to the ones reported in surface science experiments, where thiolate SAMs were irradiated in vacuum with x-rays and low energy electrons (<50 eV). According to a series of publications by Zharnikov and Grunze[48–50], the SAMs selected for our study respond differently to irradiation with x-rays or low energy electrons. HDT is prone to hydrogen abstraction, dissociation of C-S and C-C bonds (mostly at the terminal C-CH_3 bond), and crosslinking within the monolayer. PFDT dissociates more efficiently than HDT, releasing fluorine, due to the high electron affinity of the fluorinated part of the molecule. The SAMs of HDT and PFDT turn gradually into an amorphous layer of saturated and unsaturated hydrocarbons. BPT forms crosslinks between the phenyl rings, resulting in a well-defined quasi-polymerized network.

All of those processes occur in a laser-irradiated plasmonic tip-sample junction, as shown in the TER spectra presented in Fig. 2. Moreover, the symptoms of sample damage increase with the incident laser power, in analogy to the dose-dependence for electron irradiation reported by Grunze and Zharnikov[48–50]. Similarity of the reaction products suggests – but does not prove – a similar reaction mechanism. Yet, there is a striking mismatch between the energies of the irradiating particles used in the surface

science experiments and in TERS: 150−1500 eV x-rays and <50 eV electrons vs. 1.96 eV photons (633 nm laser light). This mismatch provokes the following question: is it physically feasible that the same excited states are involved in both scenarios?

In fact, reactions induced in SAMs by x-ray irradiation are governed by secondary electrons scattered off the metallic substrate, not by the primary x-ray beam[51–53]. Similarly, 10 eV electron beams cause much more damage to alkanethiolate SAMs than 2 keV electrons[54]. Secondary electrons with low energies (typically 8-20 eV) can fill antibonding molecular orbitals (Feshbach resonances) of organic adsorbates, causing their dissociation. However, reactions similar to the ones reported in this paper involve even lower electron energies: dehydrogenation of alkanethiolate SAMs by electron beams was reported for 7 eV electron beams[55,56], and loss of terminal –COOH groups was observed upon irradiating carboxyl SAMs with 0.2 eV electrons[57]. Similarly, crosslinking in bi- and ter-phenyl SAMs was induced by irradiation with 3-10 eV electrons[49,58,59]. Many more examples of chemical reactions induced by electrons with very small kinetic energies can be found in literature on electron stimulated desorption (*e. g.* dissociation of CO and NH_3 [60]), electron capture dissociation (*e. g.* fragmentation of peptides[61,62]), and dissociative electron attachment (*e. g.* radiation damage in DNA[63]).

Illumination of noble metal nanostructures with visible light results in the formation of hot carriers with energies of a few eV above the Fermi level. Excited state energies involved in plasmon-induced reactions reach 1.7 eV above Fermi level for H_2 dissociation[64] and 2.4 eV for O_2 dissociation[4]. However, the energies of hot electrons may be much higher: in particular, upon illumination with intense pulsed laser light, the hot electrons may even be photoejected from the metal (strong field emission), as demonstrated in recent experiments[65–67].

Precise determination of the excited state energies involved in the presented reactions of organic SAMs would involve calculation of the interfacial energetics of those molecular adsorbates, similar to the analysis performed for H_2[64]. This would require extensive computational effort and lies beyond the scope of this paper. Yet, the discussion above, and the results presented in Fig. 3, illustrate the fact that both electron beams and continuous irradiation with visible light can result in cascades of secondary/hot electrons in the irradiated metal, with a continuous energy spectrum up to a few eV above the Fermi level. We propose that these electrons drive similar chemical reactions in molecular adsorbates.

In our study, we apply a small tip-sample bias of 0.1 V, in order to exclude charge transfer via alternative mechanisms. Firstly, inelastic electron tunneling could occur at higher voltages, matching the energy of the vibrational modes[68]. Similarly, voltage-dependent vibrational pumping has been demonstrated in a SERS study of single Au nanoscale junctions[69]. Independent of these resonance phenomena, application of an extra potential to the plasmonic junction may simply promote carrier injection, and thus accelerate or inhibit the reported reactions. Such behavior has been observed in scanning electrochemical microscopic studies of catalysis on Au nanoparticles[25], as well as in recent electrochemical SERS[45] and TERS[70] experiments.

Phonon-driven vs. electron-mediated processes

Here we visualize the competition between hot-carrier-driven and thermally induced reactions. We take benzyl mercaptan (BM) as a model case because: (*i*) TERS/SERS triggers well-defined reactions in BM SAMs, causing reproducible changes in several vibrational modes; (*ii*) irradiated BM forms crosslinks, which prevent release of

fragments from the sample; (*iii*) BM desorbs from Au at ~380 K, which is in the range of the sample heater used in our experiment.

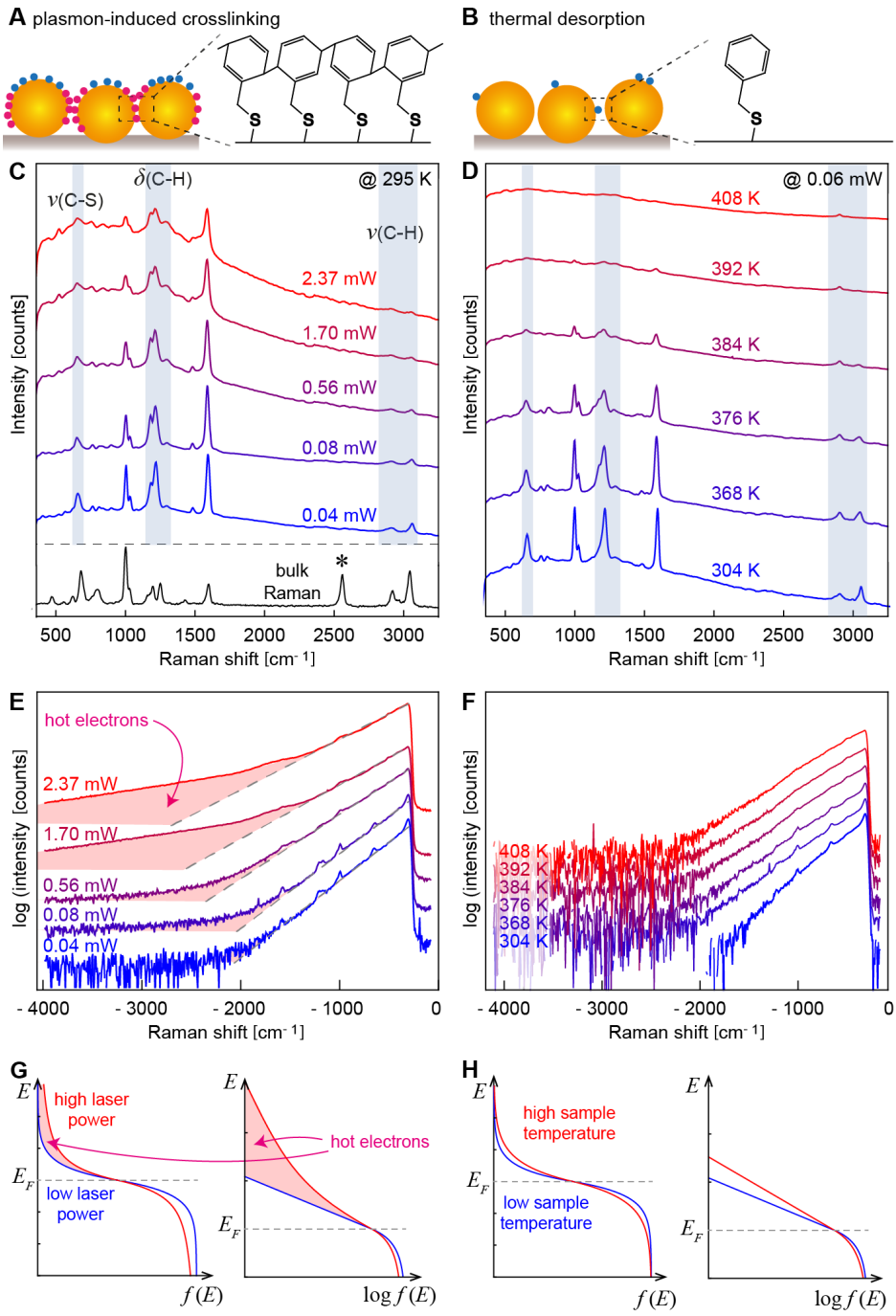

Figure 3. Hot-electron-induced vs. thermally driven reactions in a BM SAM. (A) Laser irradiation of a SERS substrate induces crosslinking in a BM SAM. (B) Heating of the BM SAM results in thermal desorption of BM. (C) SER spectra acquired at increasing laser power show that crosslinking in the BM monolayer progresses with laser power. (D) SER spectra obtained at increasing sample temperature show no crosslinking, only sample desorption around 376 K, resulting in decreased intensity of the SERS

peaks. (E) Hot electrons (light red fill) appear in the aS counterparts of the spectra from Fig. C. The contribution of the hot carriers increases with the laser power and correlates with the progress of crosslinking in the BM SAM. (F) Temperature-dependent aS-TER spectra of the BM SAM reveal negligible contribution of electrons with non-thermal energies. (G) Electronic energy E in a plasmonic hot spot follows the Fermi-Dirac distribution (blue line) for low intensity of laser illumination. The energy distribution at high laser intensities (red line) is characterized by two temperatures that appear as two linear slopes, when plotted on a logarithmic scale. A sustained population of hot carriers is marked with a light red fill. (H) Electronic energy E in a plasmonic hot spot irradiated with low laser power follows single-temperature Fermi-Dirac statistics (red and blue lines). The spectra in Fig. C, D, E, F are offset for better visibility (but not scaled).

Fig. 3 demonstrates that hot-carrier-induced and thermally driven reactions in a BM SAM lead to different products. Intense laser irradiation of the SERS substrate results in crosslinking of the monolayer (Fig. 3A), whereas heating of the sample causes desorption of the SAM (Fig. 3B). Laser-induced crosslinking of the aromatic rings in BM results in weakening of the ring breathing modes at 1000 cm^{-1}, broadening of the ring stretching band at 1600 cm^{-1}, loss of the aromatic C-H stretching vibrations at 3040 cm^{-1}, and damping of the ν(C-S) vibration at 660 cm^{-1} (Fig. 3C). Crosslinking elevates the content of sp^3-hybridized carbon in the monolayer, hence the aliphatic ν(C-H) band at 2900 cm^{-1} grows, whereas the δ(C-H) band at 1210 cm^{-1} splits into three peaks. The new peaks at 1190 cm^{-1} and 1290 cm^{-1} correspond to in-plane and out-of-plane C-H bending of sp^3-hybridized carbon atoms in the rings. Similar spectral changes are observed in TERS, at the level of a single hot spot (see Fig. S18A).

Fig. 3D shows the response of the BM SAM to an increase of sample temperature. No evidence of crosslinking in the SAM is observed, while the sample temperature is ramped up to 413 K. Instead, the intensities of all peaks start to decrease at ~370 K, when BM desorbs from the sample surface. The temperature-dependent SERS data

agree with the control TPD-MS measurements of BM (Fig. S5), where no cross-linked species were released from the SAM upon thermal desorption. Temperature-dependent TERS (Fig. S18C) shows a decrease of BM peaks upon sample desorption, similar to SERS. Yet, in TERS, additional broad bands at 1250, 1550 and 2900 cm^{-1} appear on top of the spectra at high temperatures, indicating buildup of amorphous carbon on the TERS tip, due to the deposition of released molecular fragments and their further degradation (see below).

Let us now restrict our attention to the aS background of the SER spectra in Fig. 3. SERS background arises mostly from inelastic light scattering off electrons in the plasmonic metal[71–74]. Other factors, like molecular vibrations or photoluminescence, also contribute to the background – yet, they are of secondary importance in our case. The reader is referred to the work of Mahajan *et al.*[75] that explains the contribution of molecular vibrations to the SERS background (which is evident in the Stokes part of the spectra), and to the papers by Huang *et al.*[76] and Liu *et al.*[77] that explain how luminescence arises in plasmonic nanostructures.

The aS counterparts of the spectra from Fig. 3C and D are presented in Fig. 3E and F, respectively. In the aS part of the spectra, the background is dominated by a temperature-dependent exponential decay, which can be approximated with a Boltzmann distribution (Fig. 3H, Fig. S9, see exact derivation in Section S4)[32,72,73]. Hence, the backgrounds are straight lines in the semilogarithmic plot in Fig. 3F, and their slopes are inversely proportional to the sample temperature. Yet, the aS backgrounds in Fig. 3E deviate from single exponentials (dashed gray lines), especially at high laser powers. A second exponential component emerges (marked with a light red fill). We interpret this extra component as a sustained population of hot carriers characterized by a high temperature of the electron gas (*cf.* Fig. 3G). These carriers have thermalized with other

hot carriers via electron-electron scattering (<1 ps time scale), but they did not yet exchange their energy with phonon-equilibrated electrons (a few ps time scale). These two distinct time scales of electron cooling form a basis of the two-temperature model[78,79], which has been widely used to describe the electron dynamics in noble metal nanoparticles[11,80,81] and thin metal films[82]. The high temperature component appears both in SERS (Fig. 3E) and TERS (Fig. S18B), and seems to follow the Boltzmann statistics (linear slope on semi-logarithmic scale). This is remarkable, however more rigorous modelling of the aS background is required to quantify the kinetics of hot electrons (see Section S4).

Appearance of the second exponential component was reported previously by Huang *et al.*, who used picosecond pulses of a 785 nm laser[83]. It was also observed (but not commented) by Hugall and Baumberg (see Fig. 3b in ref. [73]), who used continuous wave illumination at 785 nm. On the contrary, a strictly single-exponential aS background was observed by Xie *et al.* on arrays of plasmonic nanostructures[32], and by Banik on a single nanodumbell[74]. Understanding and quantification of the extra component in the aS background is a matter of current debate in the field. Its presence/absence may depend on the excitation wavelength and the band structure of the metal (possible interband transitions). Importantly, an apparent biexponential aS background could also arise as an artifact, for example for bimetallic SERS substrates (the two temperatures would then correspond to the two metals), or simply due to incorrect subtraction of the noise from the spectra.

A fit of a two-temperature model (sum of the two Boltzmann distributions, see Fig. S10) to the spectrum acquired at 2.37 mW (Fig. 3E) yields an effective temperature of 1630 ± 30 K for the hot electrons and a macroscopic temperature of 440 ± 4 K for the electrons equilibrated with phonons. The high-temperature Boltzmann component

constitutes 16.1 $\pm$ 0.5 % of the entire aS background. This is the share of hot electrons in the total population of electrons in the hot spot, measured at steady state. The reported value is insanely high, taking into account the very fast decay of hot carriers. It may be overestimated, due to oversimplified fitting procedure (see Section S4). However, hot electron shares of a few percent were recently reported by Sheldon *et al.*[84], who used a more rigorous implementation of the two-temperature model.

The temperature increase in the hot spot is also reflected in the aS/S peak ratios. Yet, these ratios are affected by wavelength-dependent factors and vibrational pumping[31,69]. These factors introduce a huge uncertainty in the measured temperatures, as discussed extensively by Pozzi *et al.*[31]. Hence, we did not use peak ratios for our temperature measurements.

Plasmon-driven crosslinking in BM apparently progresses with laser power, while the total deposited energy and the residence time of the sample in the hot spot are of secondary importance during a TERS experiment (Fig. S17). The reactions triggered on SERS substrates (Fig. 3) can also occur under the TERS tip (Fig. S18). Comparison of the aS background acquired with SERS and TERS on the BM SAM reveals that the background is well defined for a single hot spot (TERS), but varies substantially over the surface of the SERS substrate (Fig. S19). This indicates that reaching product selectivity in plasmon-assisted photocatalysis requires development of much more uniform plasmonic substrates.

Formation of side products

The above example illustrates that plasmon-induced hot carriers can open novel reaction pathways, which are not accessible thermally. Directing the reaction towards one specific pathway would require precise control of the hot carrier energy

distribution, which is not possible to date using continuous wave illumination. Hence, along with the desired products, side products always form in hot-electron-driven reactions. Here we investigate one class of side reactions, formation of amorphous carbon ($(CH_x)_n$, $0.2 \leq x \leq 1.0$), which is observed in both plasmon-induced photocatalysis[4], and conventional catalytic conversion (fouling), and may lead to deactivation of the catalyst[85]. It is also an undesired effect in SERS and TERS, where chemical transformations of molecules in the hot spot are perceived as sample degradation. Similar to the well-defined electron-induced reactions discussed above, there is a remarkable analogy between deposition of carbon in plasmonics and in x-ray/e-beam experiments.

Fig. 4 illustrates the formation of amorphous carbon under the TERS tip, exemplified for a SAM of thiophenol. The spectrum of the thiophenol SAM on Au is initially clean (blue spectrum, 0 s), but upon prolonged laser irradiation (2.8 mW) becomes dominated by parasitic spectral features, appearing at random positions, mostly between 1200 and 1700 cm^{-1} (red spectra, 18-297 s). These features fluctuate, because they represent a mix of various transient products of sample degradation, presumably polycyclic aromatic hydrocarbons (PAHs, see Fig. S20). The fluctuating peaks do not appear at reproducible positions, hence averaging them yields two broad background humps (dashed black line), resembling the spectrum of amorphous carbon (top black line, confocal Raman spectrum of carbon nanopowder), with peaks of intact thiophenol sitting on top of the background (dark red spectrum). The background increases with exposure time and eventually dominates the spectrum (black spectrum, 400 s), indicating buildup of a layer of amorphous carbon on the TERS tip. The carbonaceous deposit can sometimes be removed during further tip scanning (Fig. S21). Regrettably, the fluctuating spectra of the transient products of sample degradation are frequently

misinterpreted as single-molecule behavior or as signatures of biomolecules[86,87]. This misconception arose in the early years of single molecule SERS[27] and persists until today. No particular examples of such papers are pointed out to avoid stigmatization of other researches.

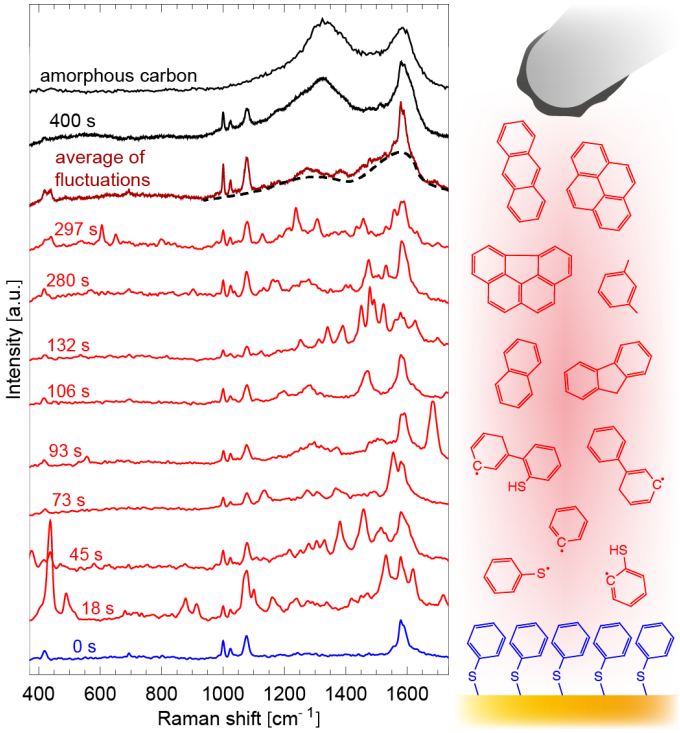

Figure 4. Fluctuating bands of carbonaceous species evolving under the TERS tip. Upon prolonged intense laser illumination (2.8 mW), a clean TER spectrum of thiophenol (blue, 0 s) becomes dominated by fluctuating parasitic features between 1200 and 1700 cm^{-1} (red spectra, exposure time 18-297 s). These spectral patterns correspond to carbonaceous products of sample degradation (tentative structures in the right panel) and eventually average to two broad background humps (dashed black line), resembling amorphous carbon (top black spectrum). A carbonaceous deposit builds up with time on the tip (black spectrum, 400 s) and dominates the signal from the sample (small peaks of thiophenol). The structures of the PAH intermediates in the right panel are tentative and cannot be determined directly from the TER spectra. The mechanism of sample carbonization does not favor any specific intermediate, therefore we show several plausible candidates.

The proposed mechanism of sample carbonization in TERS is similar to the one known from scanning electron microscopy (SEM)[88] and x-ray photoelectron spectroscopy[89].

Adsorbates released from the sample surface and volatile hydrocarbons floating in the SEM chamber serve as precursors for the buildup of amorphous carbon by the scanning electron beam[88], driven by the secondary electrons scattered off the substrate[53,90]. Below we show that this is also the case in plasmonics, where appearance of carbonaceous species in the hot spot coincides with the release of sample fragments from the surface.

In order to understand the connection between sample desorption and formation of carbonaceous species in the hot spot, we performed TPD-MS and temperature-ramped SERS (allowing better control of sample temperature than TERS) on SAMs of four thiols: thiophenol, BM, benzeneselenol and BPT. Total ion current in TPD-MS (Fig. 5A) shows that the four thiols have very different desorption characteristics, despite the similar chemistry of their tail groups. The SERS signal (Fig. 5B) originates from molecules that are still adsorbed to the sample surface. It anti-correlates with the desorption rate in TPD-MS, within the temperature range of the SERS sample heater (296–416 K). Red histograms in Fig. 5C represent the number of spectra with fluctuating features as a function of sample temperature, indicating the formation of carbonaceous species, according to the mechanism illustrated in Fig. 4. This number increases together with the rate of sample desorption (*cf.* Fig. 5A), until most of the molecules have desorbed from the surface (SERS intensity below 50%, *cf.* Fig. 5B). Then, the fluctuation rate decreases, until no more material is left on the sample surface. Very few fluctuating spectra were observed for BPT, because its desorption temperature lies above the range of the sample heater used in the SERS measurements (grey background fill in Fig. 5).

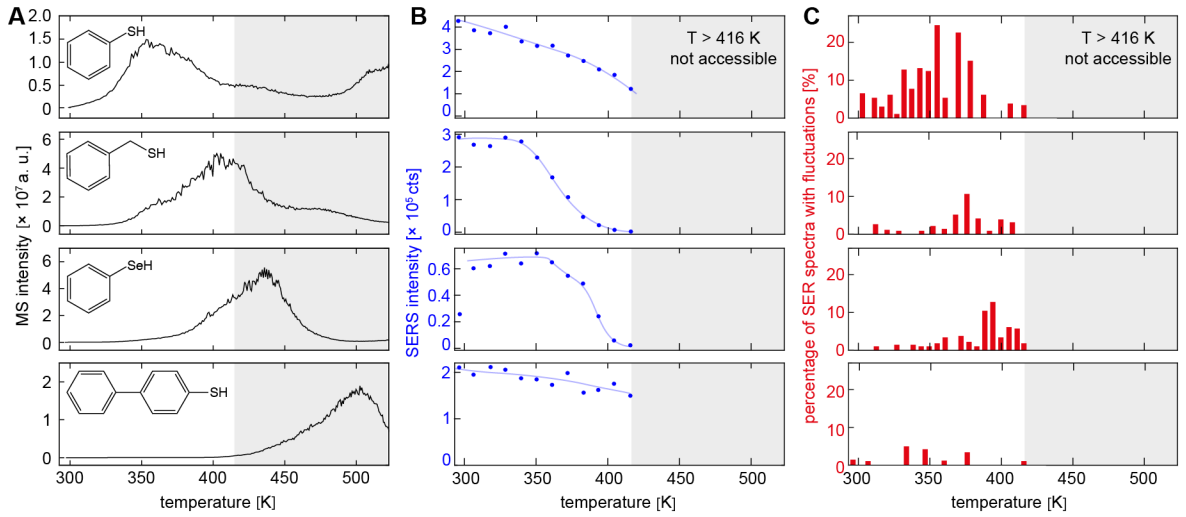

Figure 5. Appearance of carbonaceous fluctuations coincides with sample desorption. (A) The extracted ion chromatogram of the TPD-MS measurements shows the rate of thermal desorption for SAMs of thiophenol, BM, benzeneselenol and BPT for temperature between 296 and 523 K. The MS intensities were obtained by summation of the peak intensities of all ions originating from the SAM (total ion current excluding setup-specific signals). (B) Temperature-dependent SERS measurements on the same SAMs show a decrease in signal intensity (blue marks) upon sample desorption, due to the decreasing number of molecules left on the substrate upon elevating the temperature. The temperature range of our SERS sample heater was 296–416 K (white background fill), hence temperatures above 416 K (grey background fill) were out of the measurement range. Light blue lines are drawn to guide the eye. (C) The red histograms represent the number of fluctuating SER spectra recorded at a given temperature divided by the number of all spectra acquired at that temperature. This fluctuation rate was determined using a machine learning approach (see Section S5). For every SAM, it increases together with the desorption rate (*cf.* A), up to a point when most (>50%) of the SAM has desorbed (*cf.* B), and there is not much material left on the substrate. Once the SAM desorbs, the fluctuations become less frequent. Complete mass spectra and TPD curves for all detected molecular ions are shown in Fig. S2-S7.

The results presented in Fig. 5 prove that the formation of carbonaceous species in plasmonic hot spots is triggered by the release of reactive molecular fragments from the sample surface in the presence of hot electrons. These species may include alkyl and aryl radicals. The experiments shown in Fig. 2 prove the availability of surface-bound alkyl and aryl radicals, which are required for the crosslinking of aliphatic and aromatic

SAMs[48,54,55,57,59]. Once desorbed, these species can further react, to form a broad scope of products, due to the random orientation and distance between the released reactants. The essential role of the hot carriers is further confirmed by the TPD-MS experiments, where desorbed species are available in large quantities, yet PAHs (naphthalene, anthracene, *etc.*) do not form (see mass spectra in Fig. S2-S7), due to the absence of hot electrons.

The presented mechanism of sample carbonization is fundamentally different from pyrolysis or combustion, since it does not involve high temperatures or oxygen. Hence, it applies also to plasmonics in aqueous or UHV environments. Figure S8 shows that the hot spot temperature in TERS experiments lies between 300 and 480 K, which is well below the temperature needed to induce pyrolysis of organic molecules ($900 - 1600$ K)[91]. Yet, such an increase of temperature in the hot spot may be enough to facilitate plasmon-driven reactions, due to high electron attachment cross-sections at elevated temperatures, as demonstrated in Fig. S22, and in line with the model proposed by Christopher *et al.*[4] and experimentally confirmed by Zhang *et al.*[24] and Yu *et al.*[25]

Conclusions

Remarkable analogies exist between plasmon-driven photocatalysis and surface photochemistry induced by irradiation with x-rays or electron beams. Formation of similar reaction products in those two scenarios coincides with the presence of electrons with similar energies (secondary electrons vs. hot electrons), and the reaction progress correlates with the dose of those electrons. Moreover, in both cases, the formation of side products (amorphous carbonaceous residue) occurs upon desorption of molecular fragments from the surface in the presence of secondary/hot electrons that drive the carbonization.

These correlations do not automatically imply the same reaction mechanism (whose demonstration was not the goal of this study). We prove that the observed reaction pathways are not thermally accessible, but we do not provide a definitive direct proof for the identity of the reaction pathways in plasmonics and e-beam experiments. Moreover, we draw conclusions regarding the general scope of plasmon-driven catalysis, based on results obtained for a limited number of stoichiometric reactions in model molecules. Keeping these limitations in mind, the presented analogy serves as the first ever *rationale* for predicting the products of plasmon-driven reactions: we propose that plasmon-induced photocatalysis is only one member of a bigger family of processes, governed by a common mechanism – desorption induced by electronic transitions[60,92] (DIET, see Fig. 6). Hence, reactions known from surface science literature, induced by electron beams in UHV conditions, can be reproduced in photocatalytic reactors, in conditions close to ambient. We propose that this analogy extends beyond e-beam and x-ray-induced surface chemistry, and also applies to chemistry trigged by ultra-short laser pulses (surface femtochemistry[79]) and to gas-phase reactions induced by low-energy electrons (electron-capture dissociation[61,62], dissociative electron attachment[63]).

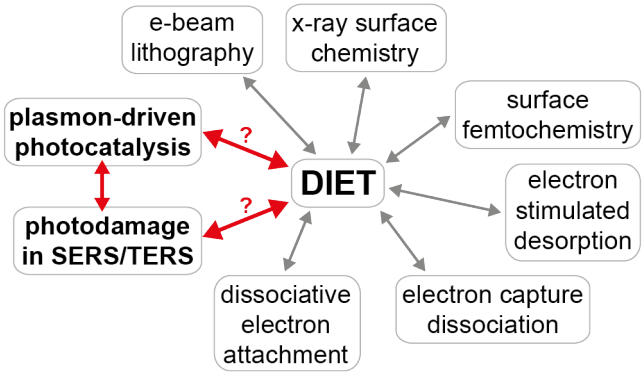

Figure 6. Our results suggest that plasmon-driven photocatalysis belongs to a bigger family of processes, governed by a common mechanism – desorption induced by electronic transitions (DIET). This analogy not only predicts the products of plasmon-driven reactions, but also explains the mechanism of photoinduced sample damage in SERS and TERS.

The intuitive link between photocatalysis and DIET has been expressed (but not documented) in the catalysis literature[8], mainly referring to surface femtochemistry experiments from the 1990s. This concept is relatively well-known among experienced researchers in catalysis. Yet, it is not realized by the vast majority of the SERS/TERS community, who frequently misinterpret spectroscopic signatures of photoinduced sample damage (see Fig. 4) as sophisticated signals from the supposedly intact sample[86,87]. The e-beam literature predicts not only the susceptibility of a given sample to hot-electron-induced damage (for example, graphene is very stable under e-beam irradiation[93], but DNA is very susceptible to DEA[63]), but also the preferred dissociation pathways. The possibility of occurrence of these reactions should be considered when interpreting SER/TER spectra that deviate dramatically from the normal Raman spectrum of the investigated sample.

The predictive power of the proposed model can be verified experimentally, contrary to any previous description of hot-electron-driven chemistry. In our next contribution we will corroborate the presented model, by showing that electron-beam-induced dissociation of peptides in the gas phase can be reproduced in a TERS hot spot.

We demonstrated that SERS/TERS can directly measure the energy of hot electrons in plasmonic nanogaps and separate charge-driven reactions from thermal processes. Moreover, we show direct measurement of the surface temperature of the plasmonic substrate. This concept can be easily implemented into catalytic reactors. Ultimately, our approach can be used for estimation of the quantum yield of hot-electron-driven reactions: the number of hot electrons can be assessed using the aS background, whereas the reaction products can be quantified using Stokes peak ratios of unreacted vs. reacted molecules, taking into account the surface coverage and the Raman cross sections.

Understanding how amorphous carbon forms in plasmonic hot spots contradicts the current paradigm ('burning'), thus providing better strategies to mitigate that process, including stabilization of the radicals evolving under the TERS tip, introduction of a drain for hot electrons, or improving energy dissipation.

Supporting Information

Supporting Information Available: materials and methods, TPD-MS measurements (complete mass chromatograms), measurement of the temperature in the hot spot using the anti-Stokes background, derivation of background fit functions (Fermi-Dirac vs. Boltzmann distribution), quantification of the share of hot electrons, comparison of the aS background in SERS and TERS, identification of fluctuations in SER spectra using a machine learning approach, TERS measurements of *n*-decanethiol, visualization of possible intermediates of sample degradation (Raman spectra of various PAHs), formation and removal of the carbonaceous deposit on the TERS tip, visualization of the interplay between charge-driven reactions and plasmonic heating.

Note

The authors declare no competing financial interest.

Acknowledgements

We thank Christian Marro from the mechanical workshop of LOC for the design and manufacturing of the desorption chamber for TPD-MS. We also thank Dr. Piotr Cyganik (Jagiellonian University), Zbigniew Wojna (University College London), Dr. András Vladár (NIST), Prof. Markus Raschke (University of Colorado), Dr. Lothar Opilik (LSPR AG, Zurich), Dr. Guillaume Goubert (LOC ETH), Jonas Metternich (LOC ETH), Prof. Matthew Sheldon (Texas A&M), Prof. V. Ara Apkarian (UC Irvine) and Steven Jones

(Chalmers Univ.) for very fruitful discussions, and Martin Gaugg (LOC ETH) for help with analysis of the MS data. The study was funded by an ETH Research Grant (project ETH-12 14-1). The data used in this publication are freely accessible from the curated data archive of ETH Zurich (https://www.research-collection.ethz.ch) under the DOI 10.3929/ethz-b-000268059.

References

(1) Liu, Z.; Hou, W.; Pavaskar, P.; Aykol, M.; Cronin, S. B. *Nano Lett.* **2011**, *11*, 1111–1116.

(2) Ingram, D. B.; Linic, S. *J. Am. Chem. Soc.* **2011**, *133*, 5202–5205.

(3) Hung, W. H.; Aykol, M.; Valley, D.; Hou, W.; Cronin, S. B. *Nano Lett.* **2010**, *10*, 1314–1318.

(4) Christopher, P.; Xin, H.; Linic, S. *Nat. Chem.* **2011**, *3*, 467–472.

(5) Christopher, P.; Linic, S. *ChemCatChem* **2010**, *2*, 78–83.

(6) Primo, A.; Corma, A.; García, H. *Phys. Chem. Chem. Phys.* **2011**, *13*, 886–910.

(7) Brongersma, M. L.; Halas, N. J.; Nordlander, P. *Nat. Nanotechnol.* **2015**, *10*, 25–34.

(8) Linic, S.; Aslam, U.; Boerigter, C.; Morabito, M. *Nat. Mater.* **2015**, *14*, 567–576.

(9) Manjavacas, A.; Liu, J. G.; Kulkarni, V.; Nordlander, P. *ACS Nano* **2014**, *8*, 7630–7638.

(10) Somorjai, G. A.; Contreras, A. M.; Montano, M.; Rioux, R. M. *Proc. Natl. Acad. Sci.* **2006**, *103*, 10577–10583.

(11) Burda, C.; Chen, X.; Narayanan, R.; El-Sayed, M. A. *Chem. Rev.* **2005**, *105*, 1025–1102.

(12) Novo, C.; Funston, A. M.; Mulvaney, P. *Nat. Nanotechnol.* **2008**, *3*, 598–602.

(13) Cheng, J.; Liu, Y.; Cheng, X.; He, Y.; Yeung, E. S. *Anal. Chem.* **2010**, *82*, 8744–8749.

(14) Zou, N.; Chen, G.; Mao, X.; Shen, H.; Choudhary, E.; Zhou, X.; Chen, P. *ACS Nano* **2018**, *12*, 5570–5579.

(15) Chen, P.; Zhou, X.; Andoy, N. M.; Han, K.-S.; Choudhary, E.; Zou, N.; Chen, G.; Shen, H. *Chem. Soc. Rev.* **2014**, *43*, 1107–1117.

(16) Ha, J. W.; Ruberu, T. P. A.; Han, R.; Dong, B.; Vela, J.; Fang, N. *J. Am. Chem. Soc.* **2014**, *136*, 1398–1408.

(17) Choi, H. K.; Park, W. H.; Park, C. G.; Shin, H. H.; Lee, K. S.; Kim, Z. H. *J. Am. Chem. Soc.* **2016**, *138*, 4673–4684.

(18) Cortés, E.; Xie, W.; Cambiasso, J.; Jermyn, A. S.; Sundararaman, R.; Narang, P.; Schlücker, S.; Maier, S. A. *Nat. Commun.* **2017**, *8*, 1–10.

(19) Wilson, A. J.; Willets, K. A. *Nano Lett.* **2014**, *14*, 939–945.

(20) Wang, X.; Huang, S.-C.; Huang, T.-X.; Su, H.-S.; Zhong, J.-H.; Zeng, Z.-C.; Li, M.-H.; Ren, B. *Chem. Soc. Rev.* **2017**, *46*, 4020–4041.

(21) Zrimsek, A. B.; Chiang, N.; Mattei, M.; Zaleski, S.; McAnally, M. O.; Chapman, C. T.; Henry, A. I.; Schatz, G. C.; Van Duyne, R. P. *Chem. Rev.* **2017**, *117*, 7583–7613.

(22) Hartman, T.; Wondergem, C. S.; Kumar, N.; Van Den Berg, A.; Weckhuysen, B. M. *J. Phys. Chem. Lett.* **2016**, *7*, 1570–1584.

(23) Harvey, C. E.; Weckhuysen, B. M. *Catal. Letters* **2015**, *145*, 40–57.

(24) Zhang, X.; Li, X.; Reish, M. E.; Zhang, D.; Su, N. Q.; Gutiérrez, Y.; Moreno, F.; Yang, W.; Everitt, H. O.; Liu, J. *Nano Lett.* **2018**, *18*, 1714–1723.

(25) Yu, Y.; Sundaresan, V.; Willets, K. A. *J. Phys. Chem. C* **2018**, *122*, 5040–5048.

(26) Nie, S.; Emory, S. *Science* **1997**, *275*, 1102–1106.

(27) Xu, H. X.; Bjerneld, E. J.; Käll, M.; Börjesson, L. *Phys. Rev. Lett.* **1999**, *83*, 4357–4360.

(28) Kurouski, D.; Mattei, M.; Van Duyne, R. P. *Nano Lett.* **2015**, *15*, 7956–7962.

(29) Zeng, Z.; Huang, S.; Wu, D.; Meng, L.; Li, M.; Huang, T.; Zhong, J.-H.; Wang, X.; Yang, Z.-L.; Ren, B. *J. Am. Chem. Soc.* **2015**, *137*, 11928–11931.

(30) Martín Sabanés, N.; Ohto, T.; Andrienko, D.; Nagata, Y.; Domke, K. F. *Angew. Chemie - Int. Ed.* **2017**, *56*, 9796–9801.

(31) Pozzi, E. A.; Zrimsek, A. B.; Lethiec, C. M.; Schatz, G. C.; Hersam, M. C.; Van Duyne, R. P. *J. Phys. Chem. C* **2015**, *119*, 21116–21124.

(32) Xie, X.; Cahill, D. G. *Appl. Phys. Lett.* **2016**, *109*.

(33) Bayle, M.; Combe, N.; Sangeetha, N. M.; Viau, G.; Carles, R. *Nanoscale* **2014**, *6*, 9157–9165.

(34) Zhang, H.; Zhang, X.-G.; Wei, J.; Wang, C.; Chen, S.; Sun, H.-L.; Wang, Y.-H.; Chen, B.-H.; Yang, Z.-L.; Wu, D.-Y.; et al. *J. Am. Chem. Soc.* **2017**, *139*, 10339–10346.

(35) van Schrojenstein Lantman, E. M.; Deckert-Gaudig, T.; Mank, A. J. G.; Deckert, V.; Weckhuysen, B. M. *Nat. Nanotechnol.* **2012**, *7*, 583–586.

(36) Sun, M.; Zhang, Z.; Zheng, H.; Xu, H. *Sci. Rep.* **2012**, *2*, 2–5.

(37) Kumar, N.; Stephanidis, B.; Zenobi, R.; Wain, A. J.; Roy, D. *Nanoscale* **2015**, *7*, 7133–7137.

(38) Sprague-Klein, E. A.; McAnally, M. O.; Zhdanov, D. V.; Zrimsek, A. B.; Apkarian, V. A.; Seideman, T.; Schatz, G. C.; Van Duyne, R. P. *J. Am. Chem. Soc.* **2017**, *139*, 15212–15221.

(39) De Nijs, B.; Benz, F.; Barrow, S. J.; Sigle, D. O.; Chikkaraddy, R.; Palma, A.; Carnegie, C.; Kamp, M.; Sundararaman, R.; Narang, P.; et al. *Nat. Commun.* **2017**, *8*, 1–8.

(40) Liu, Z.; Ding, S.-Y.; Chen, Z.-B.; Wang, X.; Tian, J.-H.; Anema, J. R.; Zhou, X.-S.; Wu, D.-Y.; Mao, B.-W.; Xu, X.; et al. *Nat. Commun.* **2011**, *2*, 305.

(41) Sprague-Klein, E. A.; Negru, B.; Madison, L. R.; Coste, S. C.; Rugg, B. K.; Felts, A. M.; McAnally, M. O.; Banik, M.; Apkarian, V. A.; Wasielewski, M. R.; et al. *J. Am. Chem. Soc.* **2018**, jacs.8b06347.

(42) Zhong, J.-H.; Jin, X.; Meng, L.; Wang, X.; Su, H.-S.; Yang, Z.-L.; Williams, C. T.; Ren, B. *Nat. Nanotechnol.* **2016**, *12*, 132–136.

(43) Kazuma, E.; Jung, J.; Ueba, H.; Trenary, M.; Kim, Y. *Science* **2018**, *360*, 521–526.

(44) Tesema, T. E.; Kafle, B.; Tadesse, M. G.; Habteyes, T. G. *J. Phys. Chem. C* **2017**, *121*, 7421–7428.

(45) Li, X.; Zhang, C.; Wu, Q.; Zhang, J.; Xu, M.; Yuan, Y.; Yao, J. *J. Raman Spectrosc.* **2018**, 1–10.

(46) Chaunchaiyakul, S.; Setiadi, A.; Krukowski, P.; Catalan, F. C. I.; Akai-Kasaya, M.;

Saito, A.; Hayazawa, N.; Kim, Y.; Osuga, H.; Kuwahara, Y. *J. Phys. Chem. C* **2017**, *121*, 18162–18168.

(47) Norrod, K.; Rowlen, K. *Anal. Chem.* **1998**, *70*, 4218–4221.

(48) Zharnikov, M.; Geyer, W.; Gölzhäuser, A.; Frey, S.; Grunze, M. *Phys. Chem. Chem. Phys.* **1999**, *1*, 3163–3171.

(49) Geyer, W.; Stadler, V.; Eck, W.; Zharnikov, M.; Gölzhäuser, A.; Grunze, M. *Appl. Phys. Lett.* **1999**, *75*, 2401–2403.

(50) Zharnikov, M.; Grunze, M. *J. Vac. Sci. Technol. B Microelectron. Nanom. Struct.* **2002**, *20*, 1793.

(51) Laibinis, P. E.; Graham, R. L.; Biebuyck, H. A.; Whitesides, G. M. *Science* **1991**, *254*, 981–983.

(52) Graham, R. L.; Bain, C. D.; Biebuyck, H. A.; Laibinis, P. E.; Whitesides, G. M. *J. Phys. Chem.* **1993**, *97*, 9456–9464.

(53) Powell, C. J.; Seah, M. P. *J. Vac. Sci. Technol. A Vacuum, Surfaces, Film.* **1990**, *8*, 735–763.

(54) Olsen, C.; Rowntree, P. A. *J. Chem. Phys.* **1998**, *108*, 3750–3764.

(55) Rowntree, P.; Dugal, P.-C.; Hunting, D.; Sanche, L. *J. Phys. Chem.* **1996**, *100*, 4546–4550.

(56) Seshadri, K.; Froyd, K.; Parikh, A. N.; Allara, D. L.; Park, U. V; Pennsyl, V.; Lercel, M. J.; Craighead, H. G. *J. Phys. Chem.* **1996**, *3654*, 15900–15909.

(57) Huels, M. A.; Dugal, P. C.; Sanche, L. *J. Chem. Phys.* **2003**, *118*, 11168–11178.

(58) Cyganik, P.; Vandeweert, E.; Postawa, Z.; Bastiaansen, Z.; Vervaecke, F.; Lievens, P.; Silverans, R. E.; Winograd, N. *J. Phys. Chem. B* **2005**, *109*, 5085–5094.

(59) Amiaud, L.; Houplin, J.; Bourdier, M.; Humblot, V.; Azria, R.; Pradier, C.-M.; Lafosse, a. *Phys. Chem. Chem. Phys.* **2014**, *16*, 1050–1059.

(60) Madey, T. E. *Science* **1986**, *234*, 316–322.

(61) Tureček, F.; Julian, R. R. *Chem. Rev.* **2013**, *113*, 6691–6733.

(62) Alizadeh, E.; Gschliesser, D.; Bartl, P.; Hager, M.; Edtbauer, A.; Vizcaino, V.; Mauracher, A.; Probst, M.; Märk, T. D.; Ptasińska, S.; et al. *J. Chem. Phys.* **2011**, *134*, 1–9.

(63) Pan, X.; Cloutier, P.; Hunting, D.; Sanche, L. *Phys. Rev. Lett.* **2003**, *90*, 4.

(64) Mukherjee, S.; Libisch, F.; Large, N.; Neumann, O.; Brown, L. V.; Cheng, J.; Lassiter, J. B.; Carter, E. A.; Nordlander, P.; Halas, N. J. *Nano Lett.* **2013**, *13*, 240–247.

(65) Dombi, P.; Hörl, A.; Rácz, P.; Márton, I.; Trügler, A.; Krenn, J. R.; Hohenester, U. *Nano Lett.* **2013**, *13*, 674–678.

(66) Dombi, P. *Adv. Imaging Electron Phys.* **2009**, *158*, 1–26.

(67) Zilio, P.; Dipalo, M.; Tantussi, F.; Messina, G. C.; De Angelis, F. *Light Sci. Appl.* **2017**, *6*, e17002-8.

(68) Stipe, B. C.; Rezaei, M. A.; Ho, W. *Science* **1998**, *280*, 1732–1735.

(69) Ward, D. R.; Corley, D. A.; Tour, J. M.; Natelson, D. *Nat. Nanotechnol.* **2011**, *6*, 33–38.

(70) Huang, S.-C.; Wang, X.; Zeng, Z.-C.; Ye, J.-Z.; Ren, B. Nanoscale Characterization of the Surface Plasmon Catalysis with Electrochemical Tip-Enhanced Raman Spectroscopy. Presented at 26th International Conference on Raman Spectroscopy, 30th Aug 2018, Jeju, South Korea.

(71) Moskovits, M. *J. Raman Spectrosc.* **2005**, *36*, 485–496.

(72) Otto, A.; Akemann, W.; Pucci, A. *Isr. J. Chem.* **2006**, *46*, 307–315.

(73) Hugall, J. T.; Baumberg, J. J. *Nano Lett.* **2015**, *15*, 2600–2604.

(74) Banik, M. SERS from the Point of View of the Molecule & the Antenna, UC Irvine, **2014**.

(75) Mahajan, S.; Cole, R. M.; Speed, J. D.; Pelfrey, S. H.; Russell, A. E.; Bartlett, P. N.; Barnett, S. M.; Baumberg, J. J. *J. Phys. Chem. C* **2010**, *114*, 7242–7250.

(76) Huang, D.; Byers, C. P.; Wang, L. Y.; Hoggard, A.; Hoener, B.; Dominguez-Medina, S.; Chen, S.; Chang, W. S.; Landes, C. F.; Link, S. *ACS Nano* **2015**, *9*, 7072–7079.

(77) Liu, J. G.; Zhang, H.; Link, S.; Nordlander, P. *ACS Photonics* **2018**, *5*, 2584–2595.

(78) Anisimov, S. I.; Kapeliovich, B. L.; Perel-man, T. L. *J. Exp. Theor. Phys.* **1974**, *66*, 375–377.

(79) Frischorn, C.; Wolf, M. *Chem. Rev.* **2006**, *106*, 4207–4233.

(80) Link, S.; El-Sayed, M. A. *J. Phys. Chem. B* **1999**, *103*, 8410–8426.

(81) Saavedra, J. R. M.; Asenjo-Garcia, A.; García De Abajo, F. J. *ACS Photonics* **2016**, *3*, 1637–1646.

(82) Groeneveld, R. H. M.; Sprik, R.; Lagendjik, A. *Phys. Rev. Lett.* **1990**, *64*, 784–787.

(83) Huang, J.; Wang, W.; Murphy, C. J.; Cahill, D. G. *Proc. Natl. Acad. Sci.* **2014**, *111*, 906–911.

(84) Sheldon, M.; Hogana, N.; Wu, S. Raman Spectroscopic Indicators of the Electronic and Phononic Temperature in Plasmonic Absorbers. Presented at 26th International Conference on Raman Spectroscopy, 27th Aug 2018, Jeju, South Korea.

(85) Butt, J. B.; Petersen, E. E. *Activation, Deactivation and Poisoning of Catalysts*; Academic Press, Inc.: San Diego, **1988**.

(86) Otto, A. *J. Raman Spectrosc.* **2002**, *33*, 593–598.

(87) Domke, K. F.; Zhang, D.; Pettinger, B. *J. Phys. Chem. C* **2007**, *111*, 8611–8616.

(88) Vladar, A.; Postek, M. *Microsc. Microanal.* **2005**, *11*, 764–765.

(89) Swift, P. *Surf. Interface Anal.* **1982**, *4*, 47–51.

(90) Postek, M. T.; Vladár, A. E.; Purushotham, K. P. Nanomanufacturing Concerns about Measurements Made in the SEM II: Specimen Contamination. In *Proc. of SPIE*; Postek, M. T., Orji, N. G., Eds.; **2013**; Vol. 8819, p 88190F.

(91) Pierson, H. O. *Handbook of Carbon, Graphite, Diamonds and Fullerenes: Processing, Properties and Applications*; Noyes Publications: Park Ridge, New Jersey, **1993**.

(92) Avouris, P.; Walkup, R. E. *Annu. Rev. Phys. Chem.* **1989**, *40*, 173–206.

(93) Meyer, J. C.; Girit, C. O.; Crommie, M. F.; Zettl, A. *Nature* **2008**, *454*, 319–322.